ACS APPLIED MATERIALS & INTERFACES

Research Article

www.acsami.org

Bicontinuous Structure of $Li_3V_2(PO_4)_3$ Clustered via Carbon Nanofiber as High-Performance Cathode Material of Li-Ion Batteries

Lin Chen,[†] Bo Yan,[†] Jing Xu,[†] Chunguang Wang,[†] Yimin Chao,[‡] Xuefan Jiang,[†] and Gang Yang*[,†]

[†]Jiangsu Key Laboratory of Advanced Functional Material, Department of Chemical and Materials Engineering, Changshu Institute of Technology, 99 South Sanhua Road, Changshu 215500, China

[‡]Energy Materials Laboratory, School of Chemistry, University of East Anglia, Norwich NR47TJ, United Kingdom

Supporting Information

ABSTRACT: In this work, the composite structure of $Li_3V_2(PO_4)_3$ (LVP) nanoparticles with carbon nanofibers (CNF) is designed. The size and location of LVP particles, and the degree of graphitization and diameter of carbon nanofibers, are optimized by electrospinning and heat treatment. The bicontinuous morphologies of LVP/CNF are dependent on the carbonization of PVP and simultaneous growing of LVP, with the fibers shrunk and the LVP crystals grown toward the outside. LVP nanocystals clustered via carbon nanofibers guarantee improving the diffusion ability of Li^+, and the carbon fiber simultaneously guarantees the effective electron conductivity. Compared with the simple carbon-coated LVP and pure LVP, the particle-clustered structure guarantees high rate capability and long-life cycling stability of NF-LVP as cathode for LIBs. At 20 C rate in the range 3.0−4.3 V, NF-LVP delivers the initial capacity of 122.6 mAh g^{-1} close to the theoretical value of 133 mAh g^{-1}, and maintains 97% of the initial capacity at the 1000th cycle. The bead-like structure of cathode material clustered via carbon nanofibers via electrospinning will be further applied to high-performance LIBs.

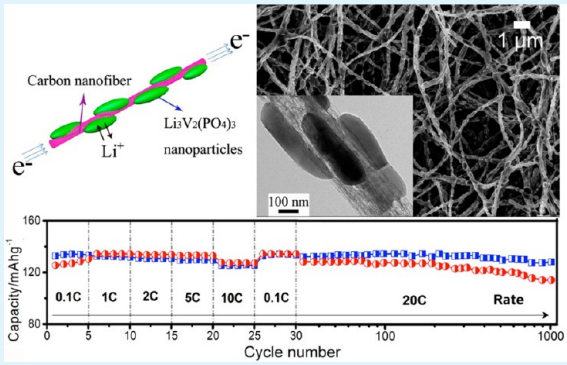

KEYWORDS: *lithium-ion batteries, cathode material, hybrid structure, nanocomposite, electrospinning*

1. INTRODUCTION

High-performance lithium-ion batteries (LIBs) have been developed as promising energy storage devices for hybrid electric vehicles (HEV) and electric vehicles (EV) owing to their high capacity, high safety, and long cycle life. Cathode materials play the key role in high-performance LIBs. In recent years, several kinds of cathode materials have been used for the increasing demand of high-performance LIBs, such as $LiCoO_2$, $LiNi_{1/3}Co_{1/3}Mn_{1/3}O_2$, $LiFePO_4$, etc., because of their competitive energy and thermal stability.[1−3]

On the basis of the crystal structure in cathode materials, the use of phosphate polyanions $(PO_4)^{3-}$ is considered to be a potential alternative for the replacement of oxide-based cathodes. The strong P−O bonds and three-dimensional solid framework in $(PO_4)^{3-}$ anions can guarantee both the dynamic and thermal stabilities required to fulfill the safety features in high-power applications.[2,3] Monoclinic Nasicon-type $Li_3V_2(PO_4)_3$ (LVP) is an attractive cathode material for LIBs, for the average 4.0 V extraction/reinsertion voltage and the high theoretical capacity of 197 mAh g^{-1} between 3.0 and 4.8 V.[4,5] However, the intrinsic low electronic conductivity of LVP critically limits its high rate performance.[5−7] To improve the conductivity and electrochemical performance, a carbon coating or graphene coating has been proven an effective way to improve the electron conductivity, but the inevitable irregular coating led to poor connectivity of the particles and hence capacity loss.[7] On the other hand, it is very popular to synthesize nanosized LVP particles by various synthesis and processing approaches. Nanosized LVP provides the short pathway during Li^+ extraction/reinsertion, but the increasingly serious aggregation will degrade the long-life cycle performance. LVP and LVP-based nanocomposites with traditional morphologies are hard to meet the demand of high-rate and long-life LIBs.[5]

Recently, combining inorganic materials with conductive architecture has attracted broad attention for enhancing lithium diffusion ability, rate ability, and cycle ability. Braun and his coworkers reported a three-dimensional (3D) silicon anode formed by depositing a layer of silicon on the surface of a porous nickel metal scaffold, maintaining the electrical connectivity during cycling.[8,9] Very recently, Mai's group reported a potential technique in synthesizing hierarchical $Li_3V_2(PO_4)_3$/carbon mesoporous nanowires. By using cetyltrimethylammonium (CTAB) and oxalic acid as surfactant and carbon sources to form the mesoporous carbon scaffolds cogrown with the crystallization of $Li_3V_2(PO_4)_3$, the conductive architecture provides 3D or 1D transport pathways for electron.[2] In the previous work, our group reported the

Received: March 29, 2015
Accepted: June 8, 2015
Published: June 8, 2015

DOI: 10.1021/acsami.5b02618
ACS Appl. Mater. Interfaces 2015, 7, 13934−13943

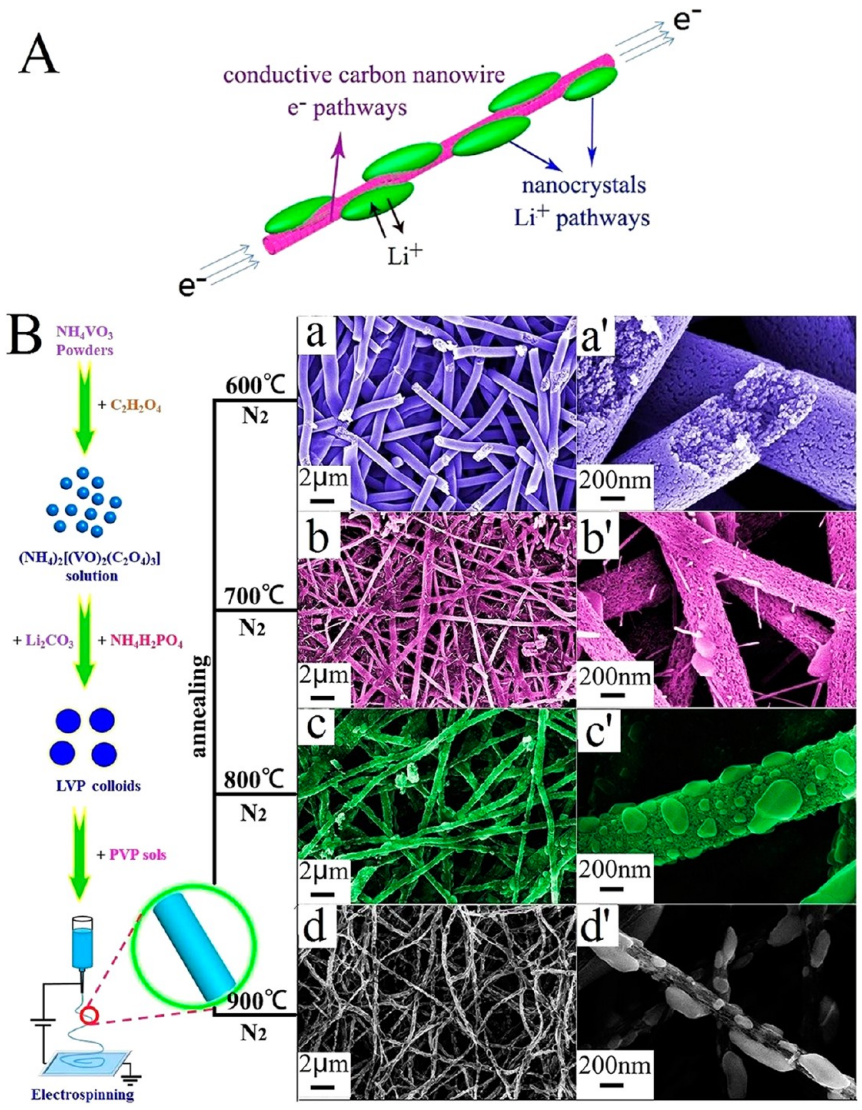

Figure 1. (A) Schematic combination of the LVP nanoparticles clustered via carbon fiber provides bicontinuous electron/ion transport pathways; (B) schematic fabrication steps and SEM images of LVP/carbon fibers after annealing at 600 °C (a, a′), 700 °C (b, b′), 800 °C (c, c′), and 900 °C (d, d′), respectively.

approaches for fabricating $Li_3V_2(PO_4)_3$ coated by conventional carbon and graphene sheets. Minor graphene effectively increased the electron conductivity of $Li_3V_2(PO_4)_3$ 3 orders of magnitude more than conventional carbon, and $Li_3V_2(PO_4)_3$/graphene presented the dramatic improvement in high-rate performance and cycling stability.[7]

Besides the improvement of the electron conductivity of $Li_3V_2(PO_4)_3$, it is also important to take the lithium diffusion ability into consideration for high-rate LIBs. Reducing the grain size to nanoscale has been proven to be an effective strategy to enhance the lithium-ion transport in electrodes, because of increasing contact surface areas between active materials and electrolyte and shortening the lithium-ion diffusion pathway.[10,11] However, the agglomeration and dissolution of nanoparticles during the charge/discharge cycles lead to reduction of electroactive sites and degradation of reversible performance.[10] In order to prevent the nanoparticles from agglomeration and dissolution during lithiation/delithiation, it is a considerable strategy that the nanoparticles are clustered along one-dimensional (1D) conductive carbon nanofiber. The assembly of nanoparticles clustered via carbon nanofiber would be an ideal microstructure to improve both electron transport and ion diffusion in the electrode materials.

The electrospinning technique as a simple and low-cost method for preparing nanofibers on a large scale has been utilized in the preparation of nanomaterials.[12−15] For example, $LiFePO_4$/C nanofibers synthesized by electrospinning showed excellent electrochemical performance.[16,17] Recently, Li and his partners prepared fibrous $Li_3V_2(PO_4)_3$/C composite, but they did not synthesize the bicontinuous structure of $Li_3V_2(PO_4)_3$ nanoparticles clustered via carbon fibers.[11] The key factor might be the fiber precursor and the following heat treatment.

In this work, we design bead-like structure of $Li_3V_2(PO_4)_3$ nanoparticles clustered via conductive carbon nanofibers. A series of $Li_3V_2(PO_4)_3$/carbon nanofibers with various morphologies are synthesized by electrospinning and heat treatment. During the in situ crystallization and carbonization processes, $Li_3V_2(PO_4)_3$ nanocrystals can be grown in nanoscale and clustered via the conductive carbon nanofibers. The particle-clustered structure not only improves ionic/electron conductivity but also inhibits $Li_3V_2(PO_4)_3$ nanoparticles trending to aggregation and inactivity during charge/discharge

DOI: 10.1021/acsami.5b02618
ACS Appl. Mater. Interfaces 2015, 7, 13934−13943

cycles. Compared with the simple carbon-coated $Li_3V_2(PO_4)_3$ and pure $Li_3V_2(PO_4)_3$, the particle-clustered structure guarantees enhanced rate capability and cycling stability. The synergetic effect of LVP and carbon fiber are studied in detail for high-performance LIBs.

2. EXPERIMENTAL SECTION

2.1. Materials Synthesis. The fabrication steps are schemed in Figure 1A. Typically, NH_4VO_3 and oxalic acid in a stoichiometric ratio of 1:3 were dissolved in deionized water under magnetic stirring at 80 °C. Stoichiometric $NH_4H_2PO_4$ and Li_2CO_3 were added to the solution, and vigorously stirred for 10 min at 80 °C. The mixture was slowly evaporated to remove part of the water for several hours until a homogeneous gel was formed. The gel was dropped slowly into the solution of 1.0 g of poly(4-vinyl) pyridine (PVP) (Alfa Aesar, M_w = 1 300 000) dissolved in 4.0 g of H_2O. The mixture was stirred for 4 h to get a homogeneous viscous solution, and was loaded into a plastic syringe equipped with a steel needle of 0.6 mm in internal diameter. The ejection rate of electrospinning was 0.25 mL h^{-1}, and the applied voltage was 20 kV. The flat aluminum foil was used to collect the composite film which was simply named LVP/PVP. After electrospinning, the composite film was removed, dried at 60 °C for 12 h under vacuum, and finally calcined for 4 h in N_2 atmosphere at a ramp rate of 2 °C min^{-1}. The as-produced $Li_3V_2(PO_4)_3$/carbon nanofibers are simply named as NF-LVP-600, NF-LVP-700, NF-LVP-800, and NF-LVP-900 according to the annealing temperature of 600, 700, 800, and 900 °C, respectively.

2.2. Materials Characterization. All X-ray studies are done on a Rigaku diffractometer (Dmax-2200) with Cu Kα radiation at 30 kV and 30 mA. The diffraction data are collected at each 0.02° step from 10° to 70°. The morphology is investigated by field emission scanning electron microscope (FE-SEM, SIGMA, ZEISS), and transmission and high-resolution transmission electron microscope (TEM, JEOL-2000CX, 200 kV and HRTEM, JEOL-2010F, 200 kV). The specific surface area was obtained from the N_2 adsorption−desorption isotherms by a Micromeritics ASAP 2020 M/C nitrogen adsorption instrument (Micromeritics Inc.) at 77 K. Raman spectra were run on a Renishaw Raman microscope. Thermogravimetric analysis (TGA) and differential scanning calorimeter (DSC) of the samples were recorded in a TG-DSC thermal analyzer system (STA449F3, NETZSCH). Carbon content was measured by VarioEL III elemental analyzer (Elementar, Germany). The electronic conductivity (σ) was obtained by the four-probe dc method. Samples were pressed into a disk of 13.0 mm diameter and ca. 0.5 mm thickness under a pressure of 50 kg cm^{-2} for 10 min, and then the sample disk was placed between two electrodes of Au sheets. The conductivity was measured by using Agilent 34401a.

2.3. Electrochemical Measurement. The electrochemical characterizations were carried out by using CR2016 coin-cell. The cathode electrode was formulated with active materials (80 wt %), Super P (10 wt %), and poly(vinylidene fluoride) (10 wt %) mixed in *N*-methyl-2-pyrrolidone. After being stirred overnight, the slurry was cast onto Al foil by using a doctor blade, and dried at 120 °C for 12 h under vacuum. The weight loading of the cathode electrode is about 4 mg cm^{-2}. The coin-cells were assembled in an argon-filled glovebox using lithium metal as the negative electrode, Celgard 2500 as the separator, and 1 M $LiPF_6$ dissolved in ethylene carbonate, dimethyl carbonate, and ethyl-methyl carbonate with a 1:1:1 volume ratio as the electrolyte. The galvanostatic charge and discharge experiments were made at room temperature (25 °C) by using LAND CT2001A (Wuhan) within the voltage range 3.0−4.3 V (1 C = 133 mAh g^{-1} vs Li^+/Li). Cyclic voltammetry (CV) was conducted on PARSTAT2273 electrochemical workstation at the scanning rate of 0.1 mV s^{-1} in the potential range 3.0−4.5 V (vs Li^+/Li). Galvanostatic intermittent titration technique (GITT) was conducted at room temperature in the voltage range 2.0−4.3 V. Electrochemical impedance spectroscopy (EIS) measures were carried out on PARSTAT2273 electrochemical workstation with sinusoidal signal of 5 mV over a frequency range from 100 kHz to 10 mHz. The state of the cell was the fifth full discharge before EIS measurement.

3. RESULTS AND DISCUSSION

The colloids of LVP are uniformly distributed in the PVP solution at first, and the precursor of LVP is dispersed in PVP to form LVP/PVP film via electrospinning (Figure 1B). PVP is used as skeleton to form mesoporous carbon nanofiber and as the carrier for captured LVP colloids. The SEM images of the LVP/PVP film present homogeneous nanofibers with the diameters about 600 nm (Supporting Information Figure S1). Under high-temperature carbonization, LVP nanoparticles cogrow with the formation of carbon fibers. TGA/DSC curves of the precursor LVP/PVP under air atmosphere are shown in Figure S2 (Supporting Information). The first weight loss of LVP/PVP below 110 °C is attributed to the molecules of LVP/PVP film physically absorbed; the second weight loss between 200 and 410 °C is attributed to the degradation of PVP molecules. The above two steps correspond to very small heat behavior. The third weight loss beyond 420 °C is attributed to the oxidation of PVP molecules corresponding to a large exothermic reaction. No weight loss appeared beyond 500 °C. Around 800 °C, there is a big exothermic peak which is attributed to the formation of $Li_3V_2(PO_4)_3$ phase.

Table 1. Results of Elemental Analysis for NF-LVPs

	C %	H %
NF-LVP-700	13.50	1.15
NF-LVP-800	12.05	1.04
NF-LVP-900	5.27	0.50

During carbonization under inert atmosphere, PVP lost the elements of N and H, converting to carbon fibers with various graphitization degrees, while LVP crystals simultaneously grow. Figure 1B shows the bicontinuous morphologies of LVP/C nanofibers produced at 700, 800, and 900 °C, respectively. Along with the increased carbonization temperature, more small molecules left, and the remaining carbon fiber was thinner; simultaneously, LVP nanoparticles grow bigger toward the outside of carbon fiber rather than the inside. As shown in the low-magnification SEM images, the three samples of NF-LVPs present long and homogeneous nanfibers. The diameters of fibers become thinner, and the surfaces of fibers become rough because small molecules are removed and bigger LVP crystals grown at higher temperature. The carbon contents are 13.50%, 12.05%, and 5.27% in NF-LVP-700, NF-LVP-800, and NF-LVP-900, respectively (as listed in Table 1). At higher magnification, the average diameters of NF-LVP-700, NF-LVP-800, and NF-LVP-900 are estimated as 430, 400, and 180 nm, respectively. LVP crystals are hardly found in carbon fibers in NF-LVP-700, but big LVP crystals grew toward the outside of carbon fiber in NF-LVP-800 and NF-LVP-900. LVP nanocrystals clustered on carbon nanofibers are propitious to improve the diffusion ability of Li^+ because of the direct contact with the electrolyte in LIBs, and the carbon fiber simultaneously guarantees the effective electron conductivity.

The X-ray diffraction (XRD) patterns of NF-LVP-600, NF-LVP-700, NF-LVP-800, and NF-LVP-900 are presented in Figure 2A. All diffraction peaks are indexed to the monoclinic LVP phase (space group $P2_1/n$) close to the lattice constants a = 8.606 Å, b = 8.592 Å, c = 12.037 Å, and β = 90.61° (JCPDS 80-1517) except NF-LVP-600. The XRD pattern of NF-LVP-

DOI: 10.1021/acsami.5b02618
ACS Appl. Mater. Interfaces 2015, 7, 13934−13943

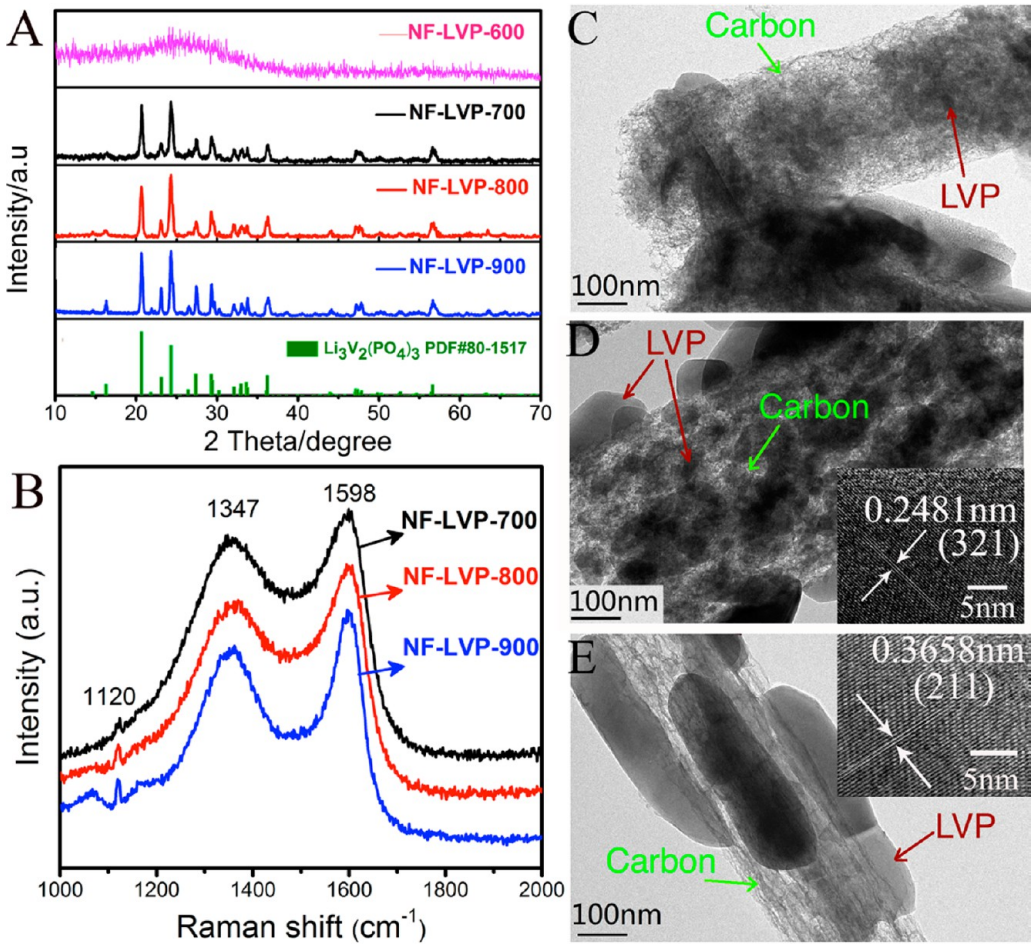

Figure 2. (A) XRD patterns of NF-LVP-600, NF-LVP-700, NF-LVP-800, NF-LVP-900, and the standard data of the $Li_3V_2(PO_4)_3$ from JCPDS 80-1517. (B) Raman spectra of NF-LVP-700, NF-LVP-800, and NF-LVP-900, respectively. TEM and HR-TEM images (the inset) of NF-LVP-700 (C), NF-LVP-800 (D), and NF-LVP-900 (E).

600 indicates the failure formation of LVP phase due to the low calcination temperature of 600 °C. The XRD patterns of NF-LVPs synthesized beyond 700 °C present high purity and crystalline LVP grown in carbon nanofibers.

Raman spectra (as shown in Figure 2B) were recorded to identify the degree of graphitization of the carbon in the samples. The two most prominent peaks at 1347 and 1598 cm^{-1} are attributed to the E_{2g} and A_{1g} vibration modes or the so-called D (disordered) and G (graphene) bands of sp^2-type carbon, respectively.[18,19] The I_D/I_G value (the peak intensity ratio between 1347 and 1598 cm^{-1} peaks) generally provides a useful index for comparing the crystallinity degree of carbon materials.[20,21] The I_D/I_G values of NF-LVP-700, NF-LVP-800, and NF-LVP-900 are 0.94, 0.90, and 0.88, respectively. The smallest I_D/I_G value 0.88 of NF-LVP-900 corresponds to the highest graphitization. Moreover, the bigger depth of the saddle between D and G peaks and the smaller value of full width at half-maximum (fwhm) of D and G bands are qualitative indicators of the highest graphitization of NF-LVP-900, suggesting that the higher temperature is beneficial to improve the degree of graphitization.[22,23] Higher carbonization temperature results in more removal of small molecules, and less carbon remained in the final products, in which the carbon contents are 13.50%, 12.05%, and 5.27% in NF-LVP-700, NF-LVP-800, and NF-LVP-900, respectively (as listed in Table 1). After the carbonation of PVP and crystallization of LVP, the elemental mapping images display the existence and uniform distribution of V, P, O, and C in NF-LVP sample (Supporting Information Figure S2).

The detailed morphologies of LVP particles in composites with carbon fibers are revealed by the typical TEM and HR-TEM images, as shown in Figure 2C–E. Small LVP nanocrystals in NF-LVP-700 and NF-LVP-800 (about 30 and 90 nm, respectively) were separately dispersed in carbon fibers, but big LVP nanoparticles in NF-LVP-900 (about 100 nm in diameter and 300 nm in length) clustered on carbon fibers. The HR-TEM images shown the insets of Figure 2D,E demonstrate the lattice fringes with the spacing of 0.248 and 0.366 nm, corresponding to the diffraction plane (321) for NF-LVP-800 and (211) for NF-LVP-900.

The Brunauer–Emmett–Teller (BET) has been employed to analyze the specific surface areas of NF-LVPs. The nitrogen adsorption–desorption isotherms with the distinct hysteresis loops can be attributed to type IV (Figure 3), and indicate a mesoporous structure.[10−13,24] The S_{BET} of NF-LVPs depends on the composite structure between LVP nanoparticles and carbon nanofibers. The specific surface areas (S_{BET}'s) of NF-LVP-700, NF-LVP-800, and NF-LVP-900 are 49.86, 58.38, and 53.01 $m^2\ g^{-1}$, respectively. NF-LVP-800 with proper LVP nanoparticles dispersed in carbon fibers exhibits the biggest S_{BET}. Because of big LVP nanoparticles on high-graphitization carbon nanofibers, NF-LVP-900 has a little lower S_{BET}. NF-

DOI: 10.1021/acsami.5b02618
ACS Appl. Mater. Interfaces 2015, 7, 13934–13943

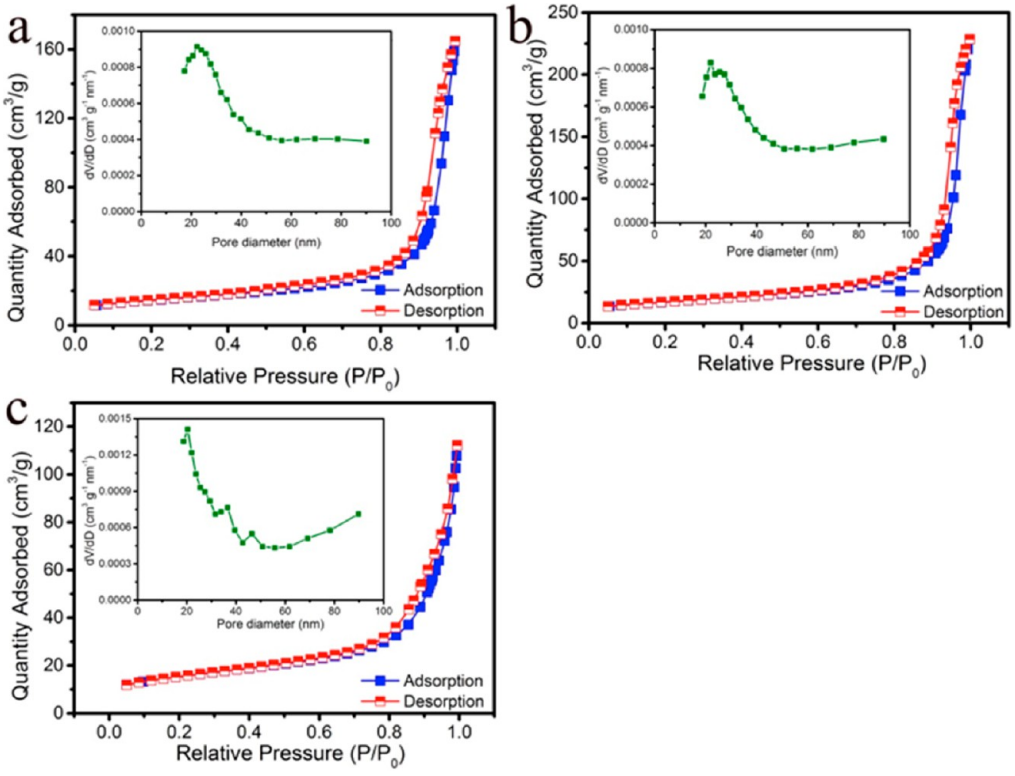

Figure 3. N_2 adsorption−desorption isotherm of (a) NF-LVP-700, (b) NF-LVP-800, and (c) NF-LVP-900. The inset in each isotherm is the corresponding pore size distributions.

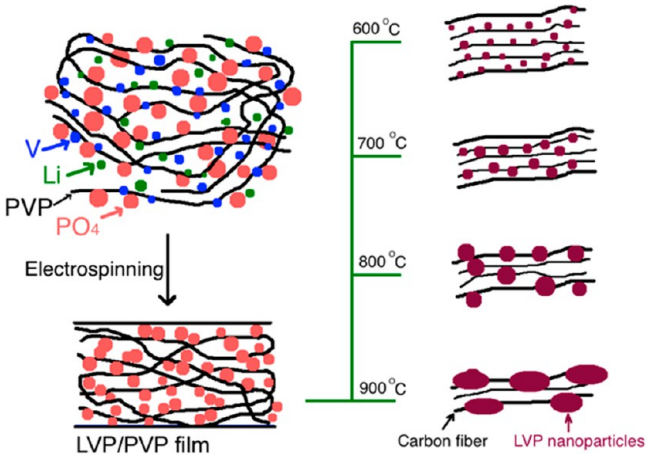

Figure 4. Proposed illustration of LVP precursor and PVP fiber, and the structure of LVP/carbon fibers after LVP/PVP is treated at various temperatures.

LVP-700 presents the lowest S_{BET} because small LVP nanoparticles are filled in the low-graphitization carbon fibers. The Barrett−Joyner−Halenda (BJH) pore size distribution curve in each isotherm indicates that the sample possesses an average pore size of about 20 nm, which might correspond to the space among the LVP/carbon fibers.

Figure 4 schematically concludes the processes of LVP clustered via carbon nanofiber. The precursor of metal salts homogeneously dissolves in the solution of PVP macromolecules. Through electrospinning, the metal salts are separately dispersed and fixed in PVP fibers. PVP fibers are like a reaction vessel; LVP precursors have to react in the limited environment. During carbonization, PVP molecules convert to carbon nanofibers, and LVP nanoparticles grow. At the beginning of carbonization, N- and H-containing small molecules are removed. The fibers of PVP are becoming thinner, and the diffusion ability of metal cations is increased to react; the primary LVP crystals are growing more. At the lowest temperature, 600 °C, carbon nanofibers appear, but the LVP phase cannot effectively grow. Along with the increased temperature, primary LVP crystals are squeezed together and grow larger accompanying the carbon nanofibers shrinking in diameter. At the temperature of 700 °C, the phase of LVP nanocrystals is grown and mainly dispersed inside carbon fibers. Beyond 800 °C, LVP crystals are further squeezed together and grow large because of the narrower carbon nanofibers. At 900 °C, a bead-like structure appears in which LVP nanocrystals are clustered via carbon nanofibers. The bicontinuous structure of LVP and carbon nanofibers possesses two advantages in electrochemical performance. For the first, LVP nanoparticles are immobile which is effective to contact electrolyte and stable during charge/discharge cycles; for the second, carbon fibers are good conductors and are accompanied by the lithiation/delithiation of LVP. The electronic conductivity (σ) was obtained by the four-probe dc method, and the calculated conductivities of NF-LVP-800 and NF-LVP-900 are 4.74×10^{-2} and 8.75×10^{-2} S cm^{-1}, respectively. Cyclic voltammetry profiles (CVs) of NF-LVP-700, NF-LVP-800, and NF-LVP-900 are plotted in Figure 5a. All the samples present three couples of redox peaks between 3.0 and 4.5 V, which reflect the diffusion ability of Li^+ extraction/reinsertion.[5,6,25,26] NF-LVP-800 and NF-LVP-900 exhibit more symmetrical and clear splitting anodic/cathodic peaks than NF-LVP-700, because the synergetic structure of LVP clustered on carbon nanofibers plays the positive role of the improved lithium diffusion ability.

DOI: 10.1021/acsami.5b02618
ACS Appl. Mater. Interfaces 2015, 7, 13934−13943

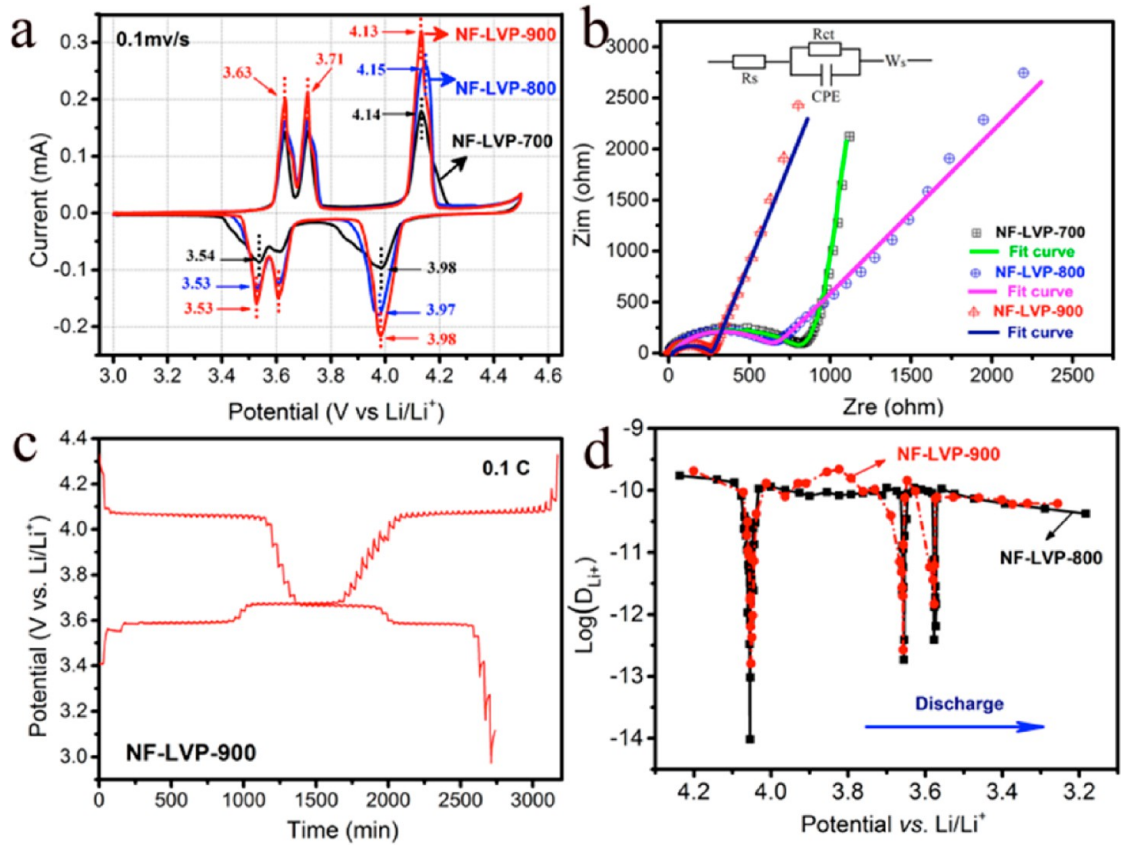

Figure 5. (a) Cyclic voltammetry profiles of NF-LVPs electrode at a scanning rate of 0.1 mV s^{-1} in the voltage range from 3.0 to 4.5 V; (b) Nyquist plots collected after the electrode worked 2 cycles at 0.1 C, and the equivalent circuit (inset) used to fit EIS; (c) GITT curves of NF-LVP-900 between 3.0 and 4.3 V (rate, 0.1 C; time interval, 30 min); (d) the diffusion coefficients of Li^+ in NF-LVP-800 and NF-LVP-900 at different discharge states.

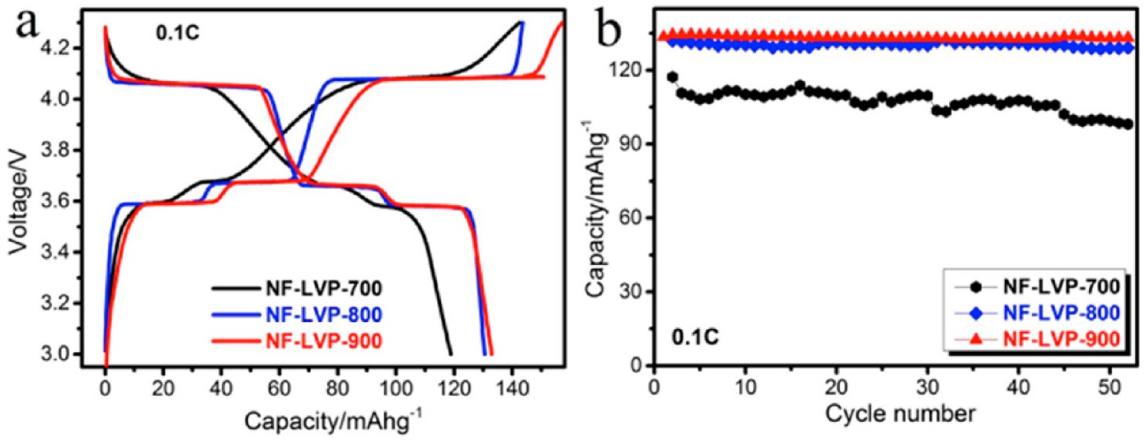

Figure 6. Initial charge/discharge profiles (a) and cycle performance (b) of NF-LVP-700, NF-LVP-800, and NF-LVP-900 in the voltage range 3.0–4.3 V at 0.1 C.

Electrochemical impedance spectroscopy (EIS) is carried out to identify the charge transfer resistance of the electrodes.[27−30] The Nyquist plots of NF-LVP-700, NF-LVP-800, and NF-LVP-900 electrodes are illustrated in Figure 5b. The EIS data are fitted by using an equivalent circuit (the inset in Figure 5b) in which R_s is the solution resistance attributed to the electrolyte and electrical contacts, R_{ct} is the charge transfer resistance from the electrolyte to the surface of cathode, accompanying the phase change of Li cations, and W_s is the Warburg resistance also known as a generalized finite Warburg element (GFW) reflects the solution of the one-dimensional diffusion equation of a particle.[31−33] The fitted values of R_s and R_{ct} are given in Table S1 (in Supporting Information). R_s values are close in the three samples. The transfer resistance (R_{ct}) of NF-LVP-900 (259 Ω) is much smaller than those of NF-LVP-700 (774 Ω) and NF-LVP-800 (627 Ω), confirming that the unique architecture of NF-LVP-900 provided the best efficiency electron/ion transport channel. GITT technique based on chronopotentiometry is further carried out to study the diffusion ability of lithium ions during charge/discharge

DOI: 10.1021/acsami.5b02618
ACS Appl. Mater. Interfaces 2015, 7, 13934−13943

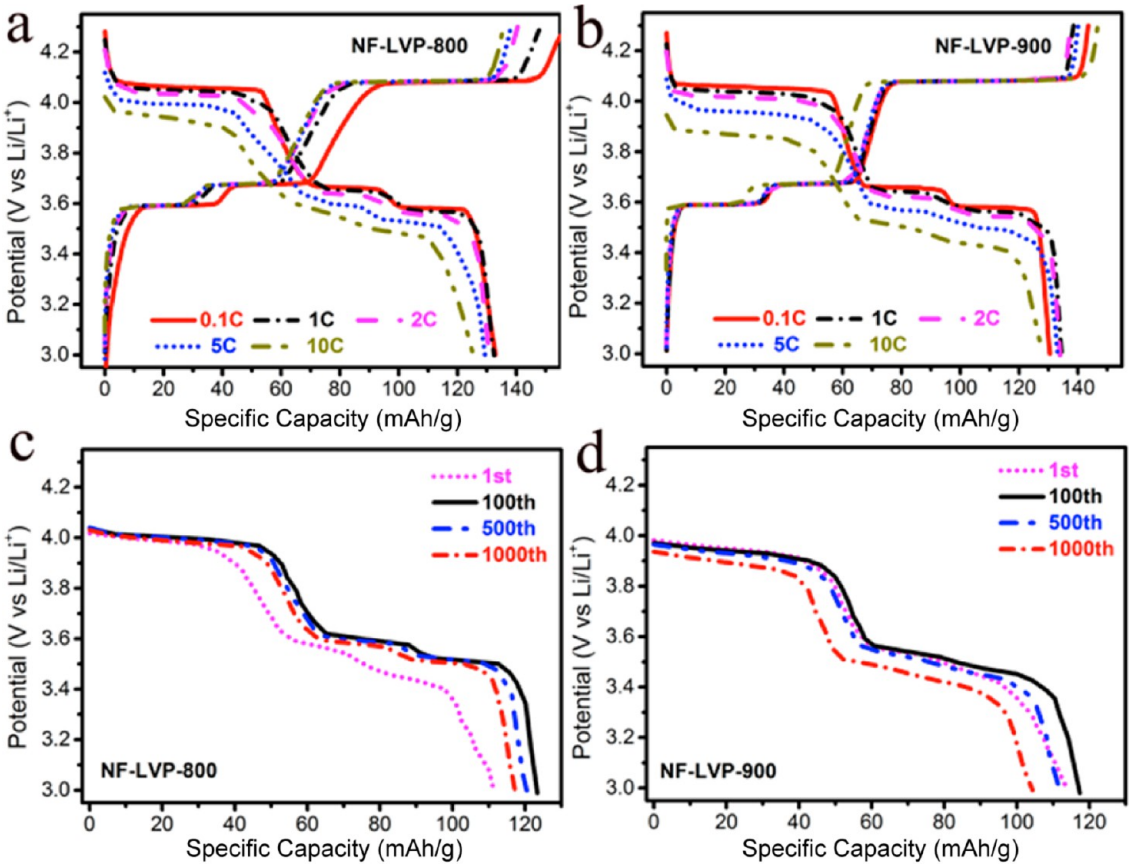

Figure 7. Electrochemical performance in 3.0−4.3 V: the initial charge/discharge profiles of NF-LVP-800 (a) and NF-LVP-900 (b) at various current rates; the discharge profiles of NF-LVP-800 (c) and NF-LVP-900 (d) at 20 C rates for 1000 cycles.

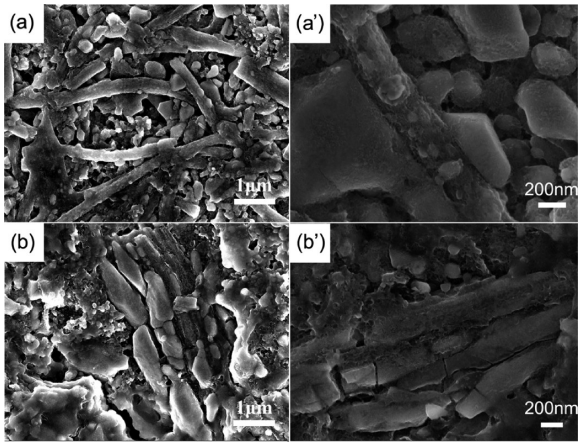

Figure 8. SEM images of (a and a′) NF-LVP-800, (b and b′) NF-LVP-900 after the 1000th cycle at 20 C rate.

processes.[34−36] The chemical diffusion coefficients is obtained by the following equation:[37−41]

$$D_{Li^+} = \frac{4}{\pi}\left(\frac{mV_M}{MA}\right)^2\left(\frac{\Delta E_S}{\tau(dE_\tau/d\sqrt{\tau})}\right)^2\left(\tau << \frac{L^2}{D_{Li^+}}\right) \quad (1)$$

Here, V_M is the molar volume of the compound, and M and m are the molecular weight and the mass of the electrode materials, respectively. A is the interface area between the active material and electrolyte. L is the average radius of the active particles. Figure 5c shows the GITT curves of NF-LVP-900 at the third charge/discharge cycle between 3.0 and 4.3 V (those of NF-LVP-800 not shown here). Thus, eq 1 is simplified as

$$D_{Li^+} = \frac{4}{\pi\tau}\left(\frac{mV_m}{MA}\right)^2\left(\frac{\Delta E_S}{\Delta E_\tau}\right)^2 \quad (2)$$

On the basis of eq 2 and GITT measurement results, D_{Li}^+ values at varied voltages during the discharge process of NF-LVP-800 and NF-LVP-900 are calculated and plotted in Figure 5d. The values of the D_{Li}^+ in NF-LVP-800 and NF-LVP-900 are close to each other, but three minimum values of D_{Li}^+ appear at the phase transition range. There is a maximum D_{Li}^+ at 3.82 V from NF-LVP-900; it might be attributed to the fact that LVP nanoparticles clustered outside carbon nanofibers in NF-LVP-900 provide good contact with electrolyte and result in better diffusion ability of Li^+. In the case of NF-LVP-800, majority LVP nanoparticles are dispersed inside with a few left on the surface of carbon nanofibers.

Figure 6 shows the initial charge/discharge curves and cyclic performance of NF-LVPs evaluated in the range 3.0−4.3 V (vs Li/Li^+). NF-LVP-800 and NF-LVP-900 deliver more than 130 mAh g^{-1} at 0.1 C (1 C =133 mA g^{-1} in 3.0−4.3 V), close to the theoretical capacity 133 mAh g^{-1} of LVP in 3.0−4.3 V. NF-LVP-800 and NF-LVP-900 present three clear couples of voltage plateaus at 3.60, 3.68, and 4.06 V, corresponding to extraction/reinsertion of 0.5 Li^+, 0.5 Li^+, and the second Li^+ of LVP.[5,6] NF-LVP-800 and NF-LVP-900 present excellent cyclic performance, which remained at 99.5% of the initial capacities after 50 cycles (as shown Figure 6b). NF-LVP-700 presents poor initial capacity of 120 mAh g^{-1} and unstable cycle stability.

DOI: 10.1021/acsami.5b02618
ACS Appl. Mater. Interfaces 2015, 7, 13934−13943

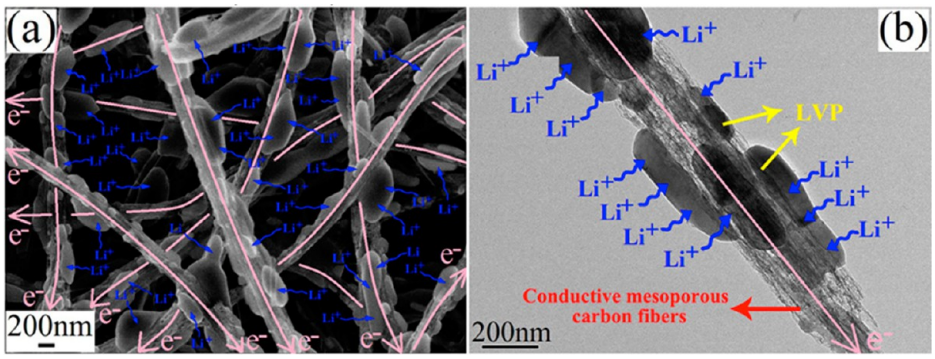

Figure 9. Scheme of bicontinuous electron/ion transport pathways drawn based on the TEM images of NF-LVP-900.

There are two main reasons: the first is that some LVP primary particles are deeply grown in carbon nanofibers and lost the chance involving the electrochemical processes; the second is that the graphitization of carbon nanofiber obtained at 700 °C is low for effective conductivity. In consideration of the poor performance of NF-LVP-700 even at 0.1 C, the following rate performances are mainly focused on NF-LVP-800 and NF-LVP-900.

Figure 7 and Figure S4 (in Supporting Information) show the initial charge/discharge profiles of NF-LVP-800 and NF-LVP-900 at 0.1, 1, 2, 5, 10, and 20 C rates, respectively. Along with the increased current rates, the voltage plateaus of LVP are relatively degraded. Until 5 C rate, both samples deliver more than 130 mAh g^{-1} (as shown in Figure 7a,b) due to LVP nanoparticles clustered on carbon fiber with the improved conductivity. For example, NF-LVP-800 delivers the initial capacities of 132.9, 132.5, 131, 129.4, and 125.4 mAh g^{-1}, and NF-LVP-900 delivers 130.5, 134.5, 133.9, 133.2, and 127.8 mAh g^{-1} at the current rates of 0.1, 1, 2, 5, and 10 C, respectively; the values are extremely close to the theoretical capacity of 133 mAh g^{-1} in 3.0−4.3 V. Besides the well-maintained discharge capacities, the clear discharge plateaus almost remain even with the discharge rate rising to 10 C (as shown in Figure 7a,b). However, the discharge voltage of 3.95 V of NF-LVP-800 is higher than 3.87 V of NF-LVP-900 at 10 C rate (estimated from discharge curves of Figure 7a,b). The little lower voltage of NF-LVP-900 might be attributed to the bigger LVP particles (about 100 nm in diameter and 300 nm in length shown in TEM images in Figure 2). The bigger LVP particles are, the slower electrochemical response is, especially at high current rate.

The bicontinuous structure of LVP nanoparticles clustered on carbon fiber improves both lithium diffusion ability and good electron conductivity. At high current rate of 20 C, LVP-800 and NF-LVP-900 reserve high performance and long-life cycling performance. As shown in Figure 7c,d, NF-LVP-800 delivers the capacities at about 120 mAh g^{-1}, and clear discharge plateaus remain at the 1000th cycle. NF-LVP-900 delivers a little lower capacity about 110 mAh g^{-1} at the 1000th cycle (Figure S4 in Supporting Information). There are comprehensive effects among the particle size, crystal morphologies, diffusion coefficient, and discharge capacities of the samples. The voltage plateaus and diffusion coefficient of lithium usually depend on the extraction/reinsertion ability of lithium in an LVP single particle; that is, smaller particles present lower polarization and bigger intrinsic D_{Li}^{+}. On the other hand, the capacity and the apparent D_{Li+} of the electrode depend on the overall abilities of lithium cation extraction/reinsertion, passing through carbon nanofiber to electrolyte. For the sample NF-LVP-900, LVP particles grown out carbon nanofibers have good contact with electrolyte. At the low current rate, NF-LVP-900 presents better electrochemical performance because the rate-determining step is the contact between LVP and electrolyte; however, at high current rate, NF-LVP-800 presents better performance because the rate-determining step is the particle size.

To view the morphologies of cycled LVP nanoparticles, the cells were disassembled after 1000 charge/discharge cycles at 20 C. The half-cell was disassembled in the glovebox, and the disassembled electrode was washed by dimethyl carbonate (DMC). The washing procedure was repeated at least three more times to remove the electrolyte from the electrode. Figure 8 shows their SEM images of NF-LVP-800 and NF-LVP-900 electrodes. NF-LVP-800 almost keeps the bicontinuous structure of LVPs composited with carbon nanofibers, but NF-LVP-900 appears as the separation of LVP nanoparticles from carbon fibers after 1000 cycles. Part of the LVP nanoparticles were cast off from NF-LVP-900 during lithiation/delithiation, because there are many LVP nanoparticles existing in the electrode. It can be concluded that the architecture of NF-LVP-800 with LVP nanoparticles clustered inside and outside of carbon nanofibers is easier to keep stable than NF-LVP-900 with most LVP particles clustered on carbon nanofibers. During charge/discharge cycles, the architecture difference gives a little larger capacity fading of NF-LVP-900 than that of NF-LVP-800 after 1000 cycles at 20 C. But the advantage of NF-LVP-900 is the lowest carbon (5.27%) content which is important for the energy density of LVP as cathode material for high-performance LIBs.

The bicontinuous nanostructure of NF-LVP-800 and NF-LVP-900 with LVP nanoparticles clustered via carbon nanofibers plays a very important role in improving and maintaining the good electrochemical performance during Li^{+} extraction/reinsertion of LVP. The 3D network by electrospun 1D geometry oriented structure, schematically shown in Figure 9 (consider NF-LVP-900 as an example), provides (i) clear channels of carbon nanofibers to guarantee the electronic conductivity; (ii) effective pathways of the clustered LVP nanoparticles via conductive carbon nanofibers for Li^{+} extraction/reinsertion to ensure the ionic conductivity; (iii) the bicontinuous nanostructure of NF-LVPs that allows the efficient contact and stability between the liquid electrolyte and the electrode.

DOI: 10.1021/acsami.5b02618
ACS Appl. Mater. Interfaces 2015, 7, 13934−13943

4. CONCLUSION

In summary, we have prepared $Li_3V_2(PO_4)_3$/carbon nanofibers (NF-LVPs) with bicontinuous structure by an electrospinning process and controllable heat treatment. LVP nanoparticles are ordered grown on high-carbonized carbon nanofibers at 900 °C. The composite structure not only improves ionic/electron conductivity but also inhibits LVP nanoparticles grown big and aggregated under a high-temperature process. The crystal morphology of LVP and carbonization degree of carbon fiber play the important roles in the composite structure and electrochemical performance. LVP nanoparticles clustered via carbon nanofibers provide bicontinuous electron/ion transport pathways, and the effective structure improves and and maintains the high rate capability and ultralong cycling stability of LVP cathode. At 20 C rate in the range 3.0−4.3 V, NF-LVP delivers the initial capacity of 122.6 mAh g^{-1} close to the theoretical value of 133 mAh g^{-1}, and a 97% capacity retention has been achieved at the 1000th cycle. The cathode nanoparticles clustered in carbon nanofibers via the strategy of electrospinning and temperature-controlled annealing process will be further applied to the field of high performance LIBs.

■ ASSOCIATED CONTENT

Ⓢ Supporting Information

Table S1 listing the fitted parameters of the samples by an equivalent circuit. Figure S1 showing the SEM images of the precursor of LVP/PVP fiber. Figure S2 showing the TGA/DSC curves of the precursor LVP/PVP under air atmosphere. Figure S3 showing the elemental mapping images of the NFPLVP-800. Figure S4 revealing the rate cyclic performance of NF-LVP-800 and NF-LVP-900. Figure S5 showing the long cyclic performance of NF-LVP-800 and NF-LVP-900 at current rate of 20 C. The Supporting Information is available free of charge on the ACS Publications website at DOI: 10.1021/acsami.5b02618.

■ AUTHOR INFORMATION

Corresponding Author

*Phone: 86-512-52251895. Fax: 86-512-52251842. E-mail: gyang@cslg.edu.cn.

Notes

The authors declare no competing financial interest.

■ ACKNOWLEDGMENTS

The work was sponsored by NSF of China (Grants 51172032, 11174043) and NSF of Jiangsu Province of China (Grant BK20141229).

■ REFERENCES

(1) Bonaccorso, F.; Colombo, L.; Yu, G. H.; Stoller, M.; Tozzini, V.; Ferrari, A. C.; Ruoff, R. S.; Pellegrini, V. Graphene, Related Two-Dimensional Crystals, and Hybrid Systems for Energy Conversion and Storage. *Science* **2015**, *347*, 6501−6509.

(2) Wei, Q. L.; An, Q. Y.; Chen, D. D.; Mai, L. Q.; Chen, S. Y.; Zhao, Y. L.; Hercule, K. M.; Xu, L.; Khan, A. M.; Zhang, Q. J. One-Pot Synthesized Bicontinuous Hierarchical $Li_3V_2(PO_4)_3$/C Mesoporous Nanowires for High-Rate and Ultralong-Life Lithium-Ion Batteries. *Nano Lett.* **2014**, *14*, 1042−1048.

(3) Saidi, M. Y.; Barker, J.; Huang, H.; Swoyer, J. L.; Adamson, G. Performance Characteristics of Lithium Vanadium Phosphate as a Cathode Material for Lithium-Ion Batteries. *J. Power Sources* **2003**, *119*, 266−272.

(4) Liu, H. D.; Gao, P.; Fang, J. H.; Yang, G. $Li_3V_2(PO_4)_3$/Graphene Nanocomposites as Cathode Material for Lithium Ion Batteries. *Chem. Commun.* **2011**, *47*, 9110−9112.

(5) Yin, S. C.; Grondey, H.; Strobel, P.; Anne, M.; Nazar, L. F. Electrochemical Property: Structure Relationships in Monoclinic $Li_{3-y}V_2(PO_4)_3$. *J. Am. Chem. Soc.* **2003**, *125*, 10402−10411.

(6) Huang, H.; Yin, S. C.; Kerr, T.; Taylor, N.; Nazar, L. F. Nanostructured Composites: A High Capacity, Fast Rate $Li_3V_2(PO_4)_3$/Carbon Cathode for Rechargeable Lithium Batteries. *Adv. Mater.* **2002**, *14*, 1525−1528.

(7) Liu, H. D.; Yang, G.; Zhang, X. F.; Gao, P.; Wang, L.; Fang, J. H.; Pinto, J.; Jiang, X. F. Kinetics of Conventional Carbon Coated-$Li_3V_2(PO_4)_3$ and Nanocomposite $Li_3V_2(PO_4)_3$/Graphene as Cathode Materials for Power Lithium Ion Batteries. *J. Mater. Chem.* **2012**, *22*, 11039−11047.

(8) Zhang, H.; Yu, X.; Braun, P. V. Three-Dimensional Bicontinuous Ultrafast-Charge and -Discharge Bulk Battery Electrodes. *Nat. Nanotechnol.* **2011**, *38*, 277−281.

(9) Zhang, H.; Braun, P. V. Three-Dimensional Metal Scaffold Supported Bicontinuous Silicon Battery Anodes. *Nano Lett.* **2012**, *12*, 2778−2783.

(10) Yang, Y.; Wang, H. Y.; Zhou, Q. W.; Kong, M. Q.; Ye, H. T.; Yang, G. Improved Lithium Storage Properties of Electrospun TiO_2 with Tunable Morphology: From Porous Anatase to Necklace Rutile. *Nanoscale* **2013**, *5*, 10267−10274.

(11) Chen, Q. Q.; Zhang, T.; Qiao, X. C.; Li, D. Q.; Yang, J. W. $Li_3V_2(PO_4)_3$/C Nanofibers Composite as a High Performance Cathode Material for Lithium-Ion Battery. *J. Power Sources* **2013**, *234*, 197−200.

(12) Wang, H. Y.; Gao, P.; Lu, S. F.; Liu, H. D.; Yang, G.; Pinto, J.; Jiang, X. F. The Effect of Tin Content to the Morphology of Sn/Carbon Nanofiber and the Performance as Anode Material for Lithium Batteries. *Electrochim. Acta* **2011**, *58*, 44−51.

(13) Hagen, R. V.; Lorrmann, H.; Moller, K. C.; Mathur, S. Electrospun $LiFe_{1-y}Mn_yPO_4$/C Nanofiber Composites as Self-Supporting Cathodes in Li-Ion Batteries. *Adv. Energy. Mater.* **2012**, *2*, 553−559.

(14) Min, J. W.; Yim, C. J.; Im, W. B. Facile Synthesis of Electrospun $Li_{1.2}Ni_{0.17}Co_{0.17}Mn_{0.5}O_2$ Nanofiber and its Enhanced High-Rate Performance for Lithium-Ion Battery Applications. *ACS Appl. Mater. Interfaces* **2013**, *5*, 7765−7769.

(15) Wu, J.; Wang, N.; Zhao, Y.; Jiang, L. Electrospinning of Multilevel Structured Functional Micro-/Nanofibers and their Applications. *J. Mater. Chem. A* **2013**, *1*, 7290−7305.

(16) Hosono, E.; Wang, Y.; Kida, N.; Enomoto, M.; Kojima, N.; Okubo, M.; Matsuda, H.; Saito, Y.; Kudo, T.; Honma, I.; Zhou, H. Synthesis of Triaxial $LiFePO_4$ Nanowire with a VGCF Core Column and a Carbon Shell through the Electrospinning Method. *ACS Appl. Mater. Interfaces* **2010**, *2*, 212−218.

(17) Zhu, C.; Yu, Y.; Gu, L.; Weichert, K.; Maier, J. Electrospinning of Highly Electroactive Carbon-Coated Single-Crystalline $LiFePO_4$ Nanowires. *Angew. Chem., Int. Ed.* **2011**, *50*, 6278−6282.

(18) Kaufman, J. H.; Metin, S.; Saperstein, D. D. Symmetry Breaking in Nitrogen-Doped Amorphous Carbon: Infrared Observation of the Raman-Active G and D Bands. *Phys. Rev. B: Condens. Matter.* **1989**, *39*, 13053−13060.

(19) Son, J. N.; Kim, G. J.; Kim, M. C.; Kim, S. H.; Aravindan, V.; Lee, Y. G.; Lee, Y. S. Carbon Coated NASICON Type $Li_3V_{2-x}M_x(PO_4)_3$ (M=Mn, Fe and Al) Materials with Enhanced Cyclability for Li-Ion Batteries. *J. Electrochem. Soc.* **2013**, *160*, A87−A92.

(20) Murugan, A. V.; Muraliganth, T.; Manthiram, A. J. Comparison of Microwave Assisted Solvothermal and Hydrothermal Syntheses of $LiFePO_4$/C Nanocomposite Cathodes for Lithium Ion Batteries. *J. Phys. Chem. C* **2008**, *112*, 14665−14671.

(21) Wang, J. W.; Zhang, X. F.; Liu, J.; Yang, G. L.; Ge, Y. C.; Yu, Z. J.; Wang, R. S.; Pan, X. M. Long-Term Cyclability and High-Rate Capability of $Li_3V_2(PO_4)_3$/C Cathode Material using PVA as Carbon Source. *Electrochim. Acta* **2010**, *55*, 6879−6884.

DOI: 10.1021/acsami.5b02618
ACS Appl. Mater. Interfaces 2015, 7, 13934−13943

(22) Doeff, M. M.; Wilcox, J. D.; Yu, R.; Aumentado, A.; Marcinek, M.; Kostecki, R. Impact of Carbon Structure and Morphology on the Electrochemical Performance of $LiFePO_4$/C Composites. *J. Solid State Electrochem.* **2008**, *12*, 995−1001.
(23) Zhou, X. F.; Wang, F.; Zhu, Y. M.; Liu, Z. P. Graphene Modified $LiFePO_4$ Cathode Materials for High Power Lithium Ion Batteries. *J. Mater. Chem.* **2011**, *21*, 3353−3358.
(24) Liu, T.; Xu, J. J.; Wu, B. B.; Xia, Q. B.; Wu, X. D. Porous $LiMn_{0.7}Fe_{0.3}PO_4$/C Prepared by a Thermal Decomposition Method as High Performance Cathode Materials for Li-Ion Batteries. *RSC Adv.* **2013**, *3*, 13337−13341.
(25) Gao, P.; Wang, L.; Chen, L.; Jiang, X. F.; Pinto, J.; Yang, G. Microwave Rapid Preparation of $LiNi_{0.5}Mn_{1.5}O_4$ and the Improved High Rate Performance for Lithium-Ion Batteries. *Electrochim. Acta* **2013**, *100*, 125−132.
(26) Mao, W. F.; Ma, Y.; Liu, S. K.; Tang, Z. Y.; Fu, Y. B. Facile Synthesis of Hybrid Phase $LiNaV_2(PO_4)_3$ and Its Application in Lithium Ion Full Cell: $Li_2NaV_2(PO_4)_3$|| $Li_2NaV_2(PO_4)_3$. *Electrochim. Acta* **2014**, *147*, 498−505.
(27) Shen, L.; Li, H.; Uchaker, E.; Zhang, X.; Cao, G. General Strategy for Designing Core-Shell Nanostructured Materials for High-Power Lithium Ion Batteries. *Nano Lett.* **2012**, *12*, 5673−5678.
(28) Gao, P.; Li, Y. H.; Liu, H. D.; Pinto, J.; Jiang, X. F.; Yang, G. Improved High Rate Capacity and Lithium Diffusion Ability of $LiNi_{1/3}Co_{1/3}Mn_{1/3}O_2$ with Ordered Crystal Structure. *J. Electrochem. Soc.* **2012**, *159*, A506−A513.
(29) Leonard, K. C.; Suyama, W. E.; Anderson, M. A. Evaluating the Electrochemical Capacitance of Surface-Charged Nanoparticle Oxide Coatings. *Langmuir* **2012**, *28*, 6476−6484.
(30) Mao, W. F.; Fu, Y. B.; Zhao, H.; Ai, G.; Dai, Y. L.; Meng, D. C.; Zhang, X. H.; Qu, D. Y.; Liu, G.; Battaglia, V. S.; Tang, Z. Y. Rational Design and Facial Synthesis of $Li_3V_2(PO_4)_3$@C Nano-Composites Using Carbon with Different Dimensions for Ultrahigh-Rate Lithium-Ion Batteries. *ACS Appl. Mater. Interfaces* **2015**, DOI: 10.1021/acsami.5b02242.
(31) Sarkar, S.; Mitra, S. $Li_3V_2(PO_4)_3$ Addition to the Olivine Phase: Understanding the Effect in Electrochemical Performance. *J. Phys. Chem. C* **2014**, *118*, 11512−11522.
(32) Kim, J. S.; Yoo, J. K.; Jung, Y. S.; Kang, K. $Li_3V_2(PO_4)_3$/Conducting Polymer as a High Power 4 V-Class Lithium Battery Electrode. *Adv. Energy Mater.* **2013**, *3*, 1004−1007.
(33) Han, D. W.; Lim, S. J.; Kim, Y.; Kang, S. H.; Lee, Y. C.; Kang, Y. M. Facile Lithium Ion Transport through Superionic Pathways Formed on the Surface of $Li_3V_2(PO_4)_3$/C for High Power Li Ion Battery. *Chem. Mater.* **2014**, *26*, 3644−3648.
(34) Yin, S. C.; Strobel, P. S.; Grondey, H.; Nazar, L. F. $Li_{2.5}V_2(PO_4)_3$: A Room-Temperature Analogue to the Fast-Ion Conducting High-Temperature γ-Phase of $Li_3V_2(PO_4)_3$. *Chem. Mater.* **2004**, *16*, 1456−1465.
(35) Chen, Q. Q.; Qiao, X. C.; Wang, Y. B.; Zhang, T. T.; Peng, C.; Yin, W. M.; Liu, L. Electrochemical Performance of $Li_{3-x}Na_xV_2(PO_4)_3$/C Composite Cathode Materials for Lithium ion. *J. Power Sources* **2012**, *201*, 267−273.
(36) Rui, X. H.; Yesibolati, N.; Li, S. R.; Yuang, C. C.; Chrn, C. H. Determination of the Chemical Diffusion Coefficient of Li^+ in Intercalation-Type $Li_3V_2(PO_4)_3$ Anode Material. *Solid State Ionics* **2011**, *187*, 58−63.
(37) Weppner, W.; Huggins, R. A. Determination of the Kinetic Parameters of Mixed-Conducting Electrodes and Application to the System Li_3Sb. *J. Electrochem. Soc.* **1977**, *124*, 1569−1578.
(38) Shi, S. J.; Tu, J. P.; Tang, Y. Y.; Zhang, Y. Q.; Wang, X. L.; Gu, C. D. Preparation and Characterization of Macroporous $Li_{1.2}Mn_{0.54}Ni_{0.13}Co_{0.13}O_2$ Cathode Material for Lithium-Ion Batteries via Aerogel Template. *J. Power Sources* **2013**, *240*, 140−148.
(39) Li, Z.; Du, F.; Bie, X. F.; Zhang, D.; Cai, Y. M.; Cui, X. R.; Wang, C. Z.; Chen, G.; Wei, Y. J. Electrochemical Kinetics of the $Li[Li_{0.23}Co_{0.3}Mn_{0.47}]O_2$ Cathode Material Studied by GITT and EIS. *J. Phys. Chem. C* **2010**, *114*, 22751−22757.
(40) Zhu, Y. J.; Wang, C. S. Galvanostatic Intermittent Titration Technique for Phase-Transformation Electrodes. *J. Phys. Chem. C* **2010**, *114*, 2830−2841.
(41) Tang, K.; Yu, X. Q.; Li, J. P.; Sun, H.; Huang, X. Kinetic Analysis on $LiFePO_4$ Thin Films by CV, GITT, and EIS. *Electrochim. Acta* **2011**, *56*, 4869−4875.

DOI: 10.1021/acsami.5b02618
ACS Appl. Mater. Interfaces 2015, 7, 13934−13943